Chinese Chemical Letters 36 (2025) 109872

Contents lists available at ScienceDirect

Chinese Chemical Letters

journal homepage: www.elsevier.com/locate/cclet

Revealing electronic state evolution of Co(II)/Co(III) in CoO (111) plane during OER process through magnetic measurement

Yanjie Li[a], Chaoqun Qu[a,*], Siqi Meng[a], Jiaqi Hu[a], Ze Gao[a,b], Hongji Xu[a], Rui Gao[a,*], Ming Feng[a,*]

[a] Key Laboratory of Functional Materials Physics and Chemistry of the Ministry of Education, Jilin Normal University, Changchun 130103, China
[b] School of Science, Changchun University of Science and Technology, Changchun 130022, China

ARTICLE INFO

Article history:
Received 12 February 2024
Revised 26 March 2024
Accepted 8 April 2024
Available online 9 April 2024

Keywords:
Oxygen evolution reaction
Cobalt oxide
Crystal plane
Electron spin state
X-ray absorption spectrum

ABSTRACT

Oxygen evolution reaction (OER) is one of the most important half-reactions related to metal-air batteries, fuel cells, and water-splitting. Due to the sluggish kinetic and multi-electron transfer, catalysts appear to be particularly important for the OER. Knowing the reaction mechanism is fundamental to developing new catalysts and improving OER efficiency. In this work, phase transition and atomic reconstruction on CoO (111) plane were revealed through *ex-situ* diffraction methods and X-ray absorption spectroscopy. At the same time, the electronic state evolution of Co(II)/Co(III) during the OER process has also been concluded by analyzing the magnetic properties. This work shows that during the OER process, Co(III) experiences surface electron rearrangement from IS (intermediate-spin state) to LS (low-spin state) and then returns to IS/HS (high-spin state) under high voltage region. This work provides a new view to reveal the reaction mechanism through the magnetic property and it can be extended to more magnetic 3d transition metals for future catalyst design.

Oxygen evolution reaction (OER) is fundamental to various clean energy technologies, such as rechargeable metal-air batteries, and electrochemical water-splitting [1,2]. However, due to the sluggish kinetic and difficulty of 4-electron charge transfer, the application of OER has been seriously restricted [3,4]. To solve these challenges, a variety of catalysts have been designed to improve the electrode kinetics and enhance stability under different electrolyte conditions [5–7], including noble metal-based materials [8–10], carbon materials [11,12] and transition metal oxides [13,14]. These catalysts make great achievements. However, there are still some issues that should be solved such as the stability of catalysts, the reaction mechanism of OER, and even the real active sites in OER process. So, it exhibits great significance to further learn the evolutions of catalysts during the electrochemical process.

Cobalt-based materials including alloys [15], oxides [16], nitrides [4,17], carbide [11], *etc.* show remarkable activity and stability of OER among 3d transition metals [18]. Compared with noble metals, they are cheaper and more stable. Numerous studies showed that the kinetic problems during the OER reaction can be further optimized by constructing cobalt-based nano-structures and tuning electron statements of Co [19–22]. For example, Ling *et al.* reported that surface atomic structure can be well-designed for superior electrocatalysis [23]. Their research shows that oxygen vacancy enriched nano fact of CoO can ensure a rapid charge transfer and accelerate OER/ORR [24]. Further study shows that not only the surface atomic density but their electron structure and coordination structure also work. By tuning the coordination environment of Co(II) vis Fe(III), Zheng *et al.* found that the OER performance could be largely enhanced [25]. Du *et al.* realize the highly stable OER process by constructing RuO_2/CoO_x composite catalysts in neutral and alkaline media [26]. This is achieved by preferential oxidation of CoO_x during OER and electron acquisition by RuO_2 through the interface. These works clearly show the application potential for cobalt-based materials from the aspect of the experiment. However, there are still some gaps to fully realize the highly efficient utilization of the catalysts. To further promote the OER performance of cobalt-based catalyst, it is of great significance to find out the reaction mechanism of cobalt-related materials during the OER process.

Recently, it has been found that most Co-based electrocatalysts will generate new phases on their surfaces during the OER process in different catalytic environments, such as strong acid or base electrolytes, and these new phases will play a more dominant

* Corresponding authors.
E-mail addresses: quchaoqun@jlnu.edu.cn (C. Qu), zjkshgr@gmail.com (R. Gao), mingfeng@jlnu.edu.cn (M. Feng).

https://doi.org/10.1016/j.cclet.2024.109872
1001-8417/

role in the electrocatalytic process [27]. Guo *et al*. designed the CoO/rGO as catalyst for OER [28]. Their work revealed that the surface of CoO will transform to Co_3O_4. Under high voltage, $CoO_x(OH)_y$ was determined as the active phase. This reaction is reversible. Zhang *et al*. find that not only CoO but Co_3O_4 will experience surface reconstruction to form a high-index plane on the surface [29]. Their work confirmed that with the existence of water Co_3O_4 can react with H_2O tuning OER performance in organic electrolytes. Ma *et al*. use the first-principle-based calculation to investigate surface reconstruction of the (111) plane in CoO [30]. It shows that the transformation from CoO_6 octahedrons to CoO_4 tetrahedrons can enhance the OER activity and the stability of O-vacancy. Their work provides a theoretical basis for developing and designing a new catalyst to enhance OER activity. From the above reports, it is acceptable that during the OER process, surface structure of cobalt oxide will experience reconstruction under alkaline electrolytes and high voltage [31]. However, the real active sites and the electronic state evolution between Co(II)/Co(III) on the surface are still not clear, especially the impact from the spin state of the electron [22,32]. To learn it well will help set up the relationship between structure and performance. Recent work about magnetic field-assisted OER catalysis inspires a new method to use the magnetic property to observe intermediate state change, which may be a good strategy to reveal the evolution of Co(II)/Co(III) from new aspects.

In the current work, (111) plane predominant cobalt oxide nanosheets were prepared through a two-step method of pyrolyzation of $Co(OH)_2$ nanosheets. Due to the high surface atomic density and enriched unsaturation edge atoms, the (111) plane exhibits excellent OER performance and benefits for the reaction mechanism study [33]. *Ex-situ* diffraction methods (XRD) and X-ray absorption spectroscopy (XAS) demonstrate the valence change of CoO during the OER reaction. It reveals the surface oxidation statement under different potentials. Transmission electron microscope (TEM) exhibits that the oxidation occurred from the edge and then extended inside the nanosheets. Most importantly, this work for the first time reveals the evolution of Co(II)/Co(III) through magnetic moment. *Ex-situ* superconducting quantum interference device (SQUID) magnetic properties further illustrate that at low voltage, CoO exhibits the high-spin (HS) statement. As the potential increased CoO was oxide to a high valance state and some CoOOH phase appeared. The electron transfer to low-spin (LS) state from HS at about 1.5 V (*vs.* RHE) and then rearrangement to intermediate-spin (IS) state to enhance the OER activity. This work reveals the electron evolution pathway during the OER process and sets up a new method to evaluate the activity of Co-based catalysts through magnetic moment measurement. Importantly, the *ex-situ* SQUID method also provides a new pathway to reveal the reaction mechanism through the calculation of magnetic moment. It can also be extended to other magnetic 3d metal systems.

The CoO nanosheets exposing (111) crystal fact are prepared through pyrolyzing single crystal $Co(OH)_2$ nanosheets. Based on the previous report, this method can not only obtain the highly exposed (111) facts but also create more unsaturated edge coordination, which will provide more surface-active sites [33]. Fig. S1 (Supporting information) exhibits the detailed structure of precursor $Co(OH)_2$ [34,35]. Calcination was controlled at 450 °C for phase transfer and at the same time kept the shape of nanosheets. Fig. 1 exhibits the microtopography of the as-prepared CoO. Figs. 1a and b are the scanning electron microscopy (SEM) images and corresponding magnification images. The size is about 5 μm in diameter and it also exhibits a shape of thin hexagon nanosheets. All the shape is well formed and uniformly distributed after calcination. Due to the porous structure, the surface is relatively rough, and the edge is jagged. Similar results can also be obtained from the atomic force microscope (AFM) images (Fig. 1c). The normalized

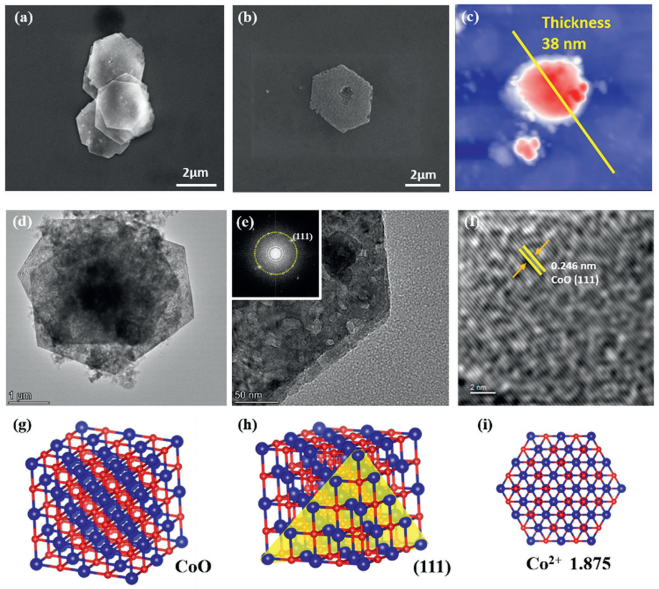

Fig. 1. (a, b) SEM images of prepared CoO and corresponding magnification image. (c) AFM contour map of CoO nanosheets. (d) TEM image of prepared CoO nanosheets. (e) HR-TEM images of CoO and the FFT of TEM images. (f) Lattice fringe image of as-prepared CoO. (g-i) Crystal cell structure and (111) plane atom schematic diagram of CoO.

thickness is 38 nm. Surface average roughness is about 2.44 nm. TEM and HR-TEM provide more detail on the edge of nanosheets. As marked in Figs. 1d and e, the nanosheets are surface enriched. From the HR-TEM, a small pore with a size of 2–3 nm shows on the surface. And the lattice parameter measured to be 2.46 Å (Fig. 1f), which can be indexed as (111) plane of CoO [30]. Fast Fourier transform is shown in the insert images of HR-TEM. It shows that all the lattice plane exposure is in [111] directions. All of the above confirmed that the CoO nanosheets exhibit thin structure and full exposure (111) facts at the same time. Moreover, it also exhibits enriched atom edges. The reason we chose it is because this plane shows the highest surface Co^{2+} density. As shown in the crystal structure diagram of (111) (Figs. 1g and h), it can expose an average of 1.875 Co^{2+} (Fig. 1i) [30].

X-ray-based methods and molecular spectrum were used to further reveal the original structure of CoO. Fig. S2 (Supporting information) shows these results. In the XRD pattern of the CoO sample (Fig. S2a), the main diffraction peaks of CoO can be found at 36.5°, 42.4°, 61.5° corresponding to the lattice plane of (111), (200), and (220) respectively, agreed with PDF #43–1004. Moreover, it was observed that due to the high exposure of (111), the XRD pattern shows a strong orientation towards the (111) plane. Compared with standard CoO, the intensity of (111) enhanced. This result further confirms the conclusion from the TEM images. As shown in Fig. S2b, the peaks centered at 190, 465, 513, and 664 cm^{-1} correspond to the characteristic peaks of CoO [33]. To further evaluate the surface valance statement, we also use X-ray absorption fine structure to detect the local structure of Co [36,37]. The pre-edge peak reflects the transition from 1s to 3d unoccupied orbit, which is related to the local geometrical configuration of Co. The main absorption edge reflects the transition from 1s to 4p unoccupied orbit, which shows the valance statement and the intensity. As can be seen from the Co XANES result (Fig. S2c), Co mainly exhibits the chemical valance statement of II. Further investigation of CoO is illustrated in Fourier-transformed R-space, which shows the local coordination number and disorder degree in CoO. It reflects the original structure of CoO before the electrochemical process. As shown in Fig. S2d. In R-space, there are two strong shells located

at 1.6 Å and 2.78 Å related to the interaction between the Co-O and Co-Co. A similar result can also be observed visually in the wavelet transformation in Figs. S2e and f.

To observe the statement evolution of Co during the OER process, a three-electrode system was employed with a glass-carbon work electrode, graphite counter electrode, and Ag/AgCl reference electrode. Rotating disk electrode (RDE) was used to evaluate the OER performance reaching a steady-state mass transport regime. It can also make the reaction stable and sufficient. 1 mol/L KOH solution was used as an electrolyte. Before the experiment, the work electrode was first activated under a non-Faraday region through cyclic voltammetry with a fast scan rate of 50 mV/s [38,39].

Linear sweep voltammetry (LSV) was performed with a scan rate of 5 mV/s (Fig. S3a in Supporting information). At a current density of 10 mA/cm^{2,} the overpotential is 0.42 V. Through the region zoom of the figure, an obvious oxidation peak appears attributed to the valance changes of Co. Based on a previous report, it is related to Co(II) → Co(III). Fig. S3b (Supporting information) shows the CV curve of CoO. As shown in the CV curve, the changes in CoO seem reversible. At 1.40 V when reverse scanning, the valance of Co reduced again. From this result, we can conclude that the CoO participated in the OER process. CoO exhibits a serious charge compensation. During the OER process, the real active site is based on the oxidated CoO surface. Tafel plot and stability measurement are shown in Figs. S3c and S4 (Supporting information), which is a reflection of OER performance.

The most important result is shown in Fig. S3d (Supporting information). It reflects the Faraday efficiency (FE) and the corresponding potential [40,41]. Through it, we can tell the reaction of cobalt oxidation and water spilling. The rotating disc ring electrode (RRDE) was used to calculate the efficiency under different potentials. The detail of method was described in detail in the experiment section. It was found that at 1.2 V, it is the non-Faraday region. So, no signal can be detected. 8% of the FE may related to some background current. The efficiency increased under 1.46 V and the FE is about 30%. It means under this potential, OER occurred with a low degree. Most of the charge was used to increase the valance of Co. When potential increases to 1.51 V, the FE reaches 41.6% confirming that there still some Co is oxidating under this potential. FE experienced a sharp increase under 1.55 V and it can reach more than 70%. To summarize, at the low potential around 1.45 V, almost all current signals come from the oxidation of surface Co. After 1.55 V, most of the charge transfers to the splitting of water. When the potential is higher than 1.6 V, more electrons transfer to the OH- and intermediate resulting in the occurrence of oxygen evolution. From the above results, it is found that under 1.5 V, charge transfer is a mixture pathway. Main of them result in oxidation of Co(II). Other reactions may include OER and some other oxygen-containing products such as H_2O_2. That also shows that the final catalyst to participate in OER reaction is the oxidation state of CoO. According to previous reports, they are Co_3O_4, and CoOOH under the alkaline solution [28]. In the current work, we mainly want to reveal the electronic state evolution between Co(II) and Co(III) in the CoO (111) plane during the OER process. In the following result, we further discuss the evolution of CoO from different aspects [28].

Fig. 2a exhibits the evolution of phases under different potentials. To make the results sensitive, we use transmission XRD with a short wavelength. As shown in the XRD pattern, three main diffraction peaks can be found belonging to CoO in the pristine CoO. It also shows that the intensity of the (111) plane increased due to the strong orientation as we described before. As the potential increased, new phases belonging to CoO(OH) appear, especially after 1.4 V. Under the potential of 1.7 V, the intensity still increased, which means the OER process can also result in Co oxidation. This result is well agreed with previous CV analysis. At the same time, XANES was also employed to detect the evolution of Co(II). Agreed with previous reports, Co will exhibit a mixture valance state of

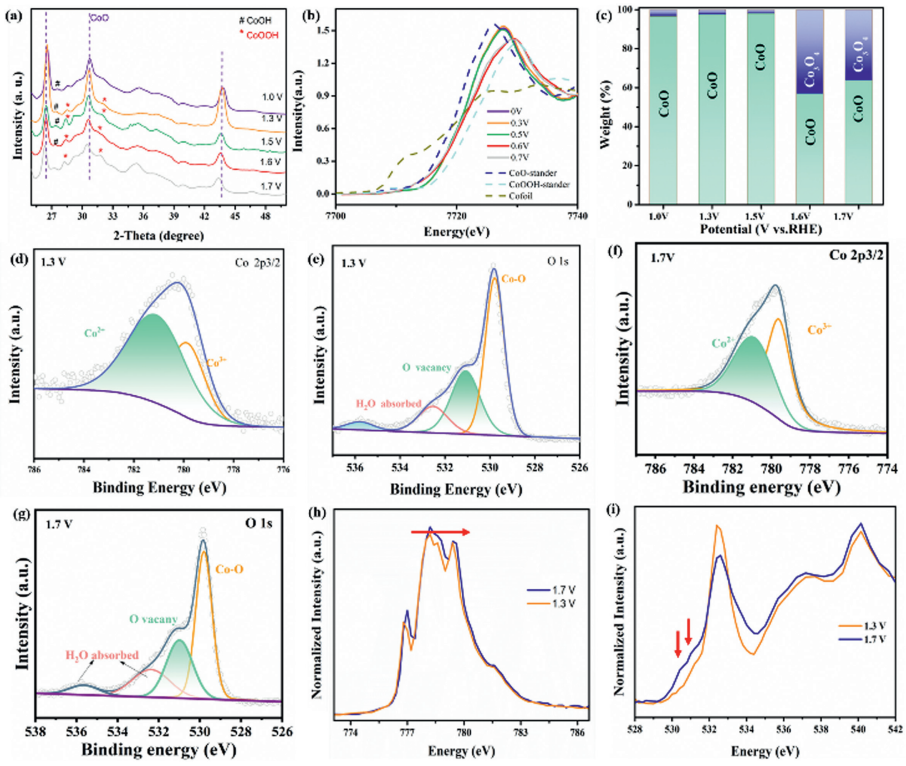

Fig. 2. (a) XRD pattern of catalysts under different potentials. (b) XANES of CoO catalysts under different potentials. (c) Linear component fitting result of CoO and Co_3O_4 for CoO catalysts under different potentials. (d, e) XPS spectra of CoO at Co 2p and O 1s region under 1.3 V. (f, g) XPS spectra of CoO at Co 2p and O 1s region under 1.7V. (h, i) Comparison of L_3-edge of Co and O-K edge at different potential.

(II) and (III) under high voltage. Figs. 2b and c show the XAFS result and the liner fitted results under different voltages [28]. In the current part, we use CoO and Co_3O_4 to reveal the changes in detail. The fitted result is shown in Fig. 2c. At high voltage, more Co(III) appears due to the strong oxidation condition. That means, at the high voltage, Co(III) plays the main role in catalyzing OER process. The absorption/desorption of intermediate products may occur on newly formed Co(III) sites. As we described before, the (111) plane shows the highest Co(II) atom density. So, it may exhibit the maximum surface oxidation. That also means using this plane to study the reaction mechanism is convincing. Moreover, it has been reported that the (111) plane is the most active index among the low-index crystal planes [29]. Fig. S5 (Supporting information) shows the corresponding FT-EXAFS data in R space. It can be seen that under 1.6 V Co-O will suffer from a large distortion due to the phase change, which is well agreed with XANES and FE results. To further reflect the surface chemical statement of Co under different voltages, we also use X-ray photoelectron spectroscopy (XPS) to reflect the binding energy. Figs. 2d and e show XPS in Co 2p and O 1s region. The energy region of Co can be fitted into 781.2 eV and 780.05 eV contributed to Co(II) and Co(III) respectively [42,43]. These results compare the Co and O under different voltages. Agreed with our previous result, the surface oxidation state is much higher at high voltage. By fitting the XPS peak, we can observe that at 1.7 V surface Co(III) increased from 20% to 30% (Figs. 2d and f). Then, we also make a detailed analysis of the O 1s region (Figs. 2e and g). Four feature peaks can be achieved belonging to lattice O (Co-O), Vacancy O, O–H, and water absorption. Compared with the pristine CoO, it is obvious that the H–O-related signal was enhanced due to the formation of CoOOH. It can be concluded that during the OER process, surface Co mainly exhibits the formation of CoOOH or hybridization Co_xO_y. This conclusion has also been confirmed by surface-sensitive soft-XAS measurement. As shown in Figs. 2h and i, the L-edge of Co and O-K edge can reflect the local structure changes of Co. Compared with the L_3-edge under 1.3 V, it shows a slight right shift of L-edge under 1.7 V indicating oxidation of Co. Moreover, the new absorption of O between 530 and 532 eV is attributed to transitions from the O 1s core level to the unoccupied t_{2g} and e_g, which reflects the existence of Co with higher valence [44].

To further reveal the reactions in space, we evaluate the changes of CoO through TEM. The results are shown in Figs. 3a and b. Under the TEM image, there seem no changes in the shape of nanosheets. After magnification of the nanosheets, the lattice parameters of CoOOH can be detected. Moreover, it can also be observed that the distribution of CoOOH appears near the edges or inner the pore. That means, the oxidation reaction is from the most active sites (edge-sites) and it gradually extends inner the nanosheets. As the reaction continues, the whole nanosheets will turn into CoOOH-dominated.

All above can roughly conclude that during the OER process, CoO will first be oxidized to a high valance state and catalyze OER. This oxidation is from the surface and coordination of unsaturated edges and then extends to the whole materials. At high voltage, with high FE, more Co(II) transforms into Co(III). All of them can well explain the result of LSV. To further confirm whether Co(II) is reversible under different electrochemical conditions, we also use the *in-situ* electrochemical quartz crystal microbalance (EQCM) to detect the mass changes during the electrochemical process [45]. Due to the mass discrepancy between CoO and CoOOH, it can to some degree reflect the reaction process of CoO. During the first process, the mass firstly experienced a sharp increase in the non-Faraday region. Based on previous results, this may attributed to the formation of $Co(OH)_2$ from CoO. As shown in Figs. 3c and d, after 1.1 V, the mass begins to decrease and after 1.5 V, the mass keeps stable. The mass flat maintained to the reverse scan and below 1.5 V, it increased sharply. Around 1.2 V, it returns to 0. And then, increased until the cycle ended. Based on the mass changes, first of all, we can conclude that the redox of Co is reversible during the first electrochemical cycle. The large mass loss is mainly attributed to the transformation from $Co(OH)_2$ to CoOOH and Co_3O_4. Under the OER process, the absorption and desorption reach balance and the phase of Co_xO_y intermediates remains stable. Similar results can also be confirmed during the second cycle, as shown in Figs. 3e and f. When the OER reaction occurs to some degree, the mass changes will reach balance and remain unchanged. As

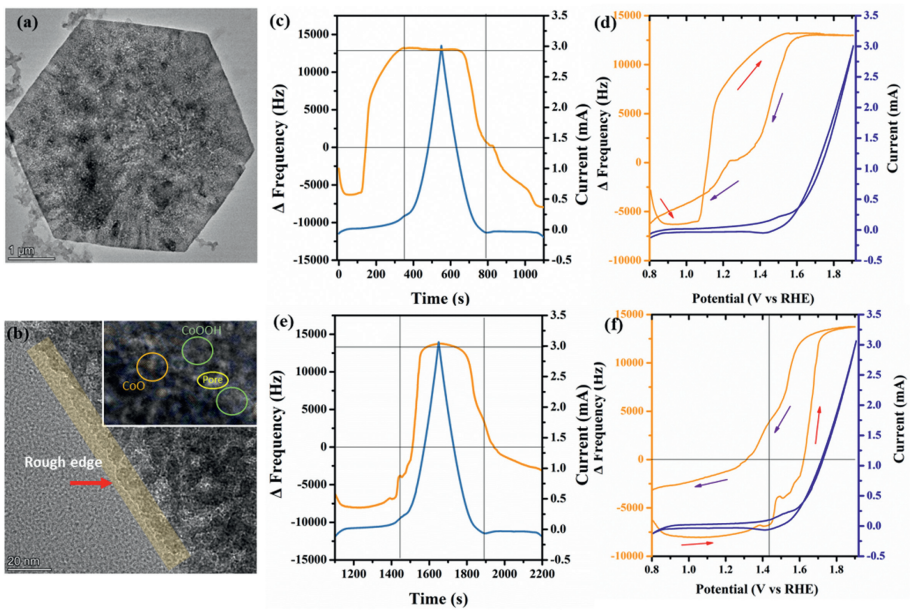

Fig. 3. (a, b) TEM and HR-TEM images after OER. (c) Time-frequency curve during CV measurement on the 1st cycle and its corresponding current curve. (d) Potential-frequency curve on the 1st cycle and its corresponding CV curve. (e) Time-frequency curve during CV measurement on the 2nd cycle and its corresponding current curve. (f) Potential-frequency curve on the 2nd cycle and its corresponding CV curve.

shown in the figure, during the second cycle, the phase changes are partially reversible. The phase changes induced in the surface reconstruction and the newly formed $Co_xO_yH_z$ compound will participate in the following reactions. That is the reason that after several cycles the performance reduced. In all during the OER process, Co(II) will experience reconstruction and oxidation. The formation of Co(III) can be described as the following reaction equation:

$$Co^{2+} + 4OH^- \rightarrow Co(OH)_4^{2-} \quad (1)$$

$$Co(OH)_4^{2-} \rightarrow CoOOH + H_2O + OH^- + e^- \quad (2)$$

Previous results reveal that during the OER process, CoO will experience the transformation to $Co(OH)_2$ and then $CoOOH/Co_3O_4$ to finally keep the high OER activity. On one hand, the valance changes have been exhibited and on the other hand, the surface conditions have also been monitored. To further investigate the performance inner the electron structure, we measure the magnetic properties of all Co-contained samples. It is well recognized that the electron arraignment can affect catalytic activity and on the other side, it can also show a change in the magnetic properties. That means, through the evolution of magnetic properties under different conditions, we can set up the relationship between electron arraignment and OER performance. Fig. 4 reflects this result and provides the electron transform process based on current results. As shown in Fig. 4a, from the H-M curve (the magnetization versus magnetic field curve), it can be concluded that pristine CoO is ferrimagnetism [46]. Bare sample exhibits the highest saturation (Msat). As the potential increased to 1.5 V and 1.6 V, it exhibits strong antiferromagnetism feature. Afterwards, it begins to return to ferrimagnetism and shows an S-shaped curve. Compared with previous results, it shows that partial surface oxidation of CoO catalyst can increase the antiferromagnetism performance. It is related to the formation of low-spin state Co(III). As the degree of oxidation extends to the whole CoO, it may change the spin state. Based on this result, we imagined the molecular magnetic dipole evolution during the OER process (Fig. 4b). In the bare CoO or under the non-Faraday region, all molecular magnetic dipoles are in the assignment of the same direction. When Co changes into Co(III), the magnetic structure changes, and some molecular magnetic dipoles point in the opposite direction. So, the magnetization intensity decreased to almost zero. As the OER process grows in depth, magnetization intensity rises again. Some molecular magnetic dipoles back to the initial direction and show higher OER performances.

This evolution of magnetic characteristics may be closely related to the electron reassignment during the phase changes. It is known that Co(II) shows only the IS state but Co(III) shows three spin-states, LS, IS, and HS [47]. It to some degree can affect the magnetic characteristic. To further reveal this process, we also use temperature-dependent magnetic moment data(M-T curve) to confirm it. By calculating the data, the magnetic torque of Co can be calculated to reflect the electron state. The result is shown in Fig. 4c depending on the potential. During the OER process, the magnetic moment decreases from 3.5 to 2.5, which corresponds to the transformation from IS-Co(II) to LS-Co(III). But under higher potential, electron spin states of Co(III) are not the final state and it will transfer to HS or IS when the potential is further increased. Based on the previous report, Co with HS state is beneficial for the OER performance [48,49]. Under this condition, though valance is still (III), the electronic state of Co(III) reassignment occurred. It transfers from LS Co(III) to IS/HS(III). All the above result confirms that during the OER process, not only the surface phase will experience reconstruction but the electron will also experience the reassignment. Under different potentials, they will exhibit different spin states as shown in Fig. 4d. That for a second time confirms that the OER performance is closely related to the HS Co(III) and in Co contained materials, it is the key factor to designing it in the materials. Moreover, this provides a new method to evaluate the catalyst by using magnetism. By monitoring the mechanism moments changes and valance state evolution, the charge transfer and electron reassignment can be well found. It should be noted that this method is not suitable for Co but for other magnetic 3d metal elements and other metals with a magnetic moment.

To summarize, this work reveals the Co(II)/Co(III) evolution of CoO during the OER process. Before reaction, Co(II) exhibits a low spin state and reflects ferromagnetism property. During the OER process, Co will first experience valence transfer from (II) to Co(III). This transformation is reversible during the first several cycles. It has been revealed in this work that under 1.5 V, IS Co(II) fast changed into LS Co(III), and the magnetic feature changed to antiferromagnetism. As potential increases, valence remains stable but the electron will transition between different orbits and finally

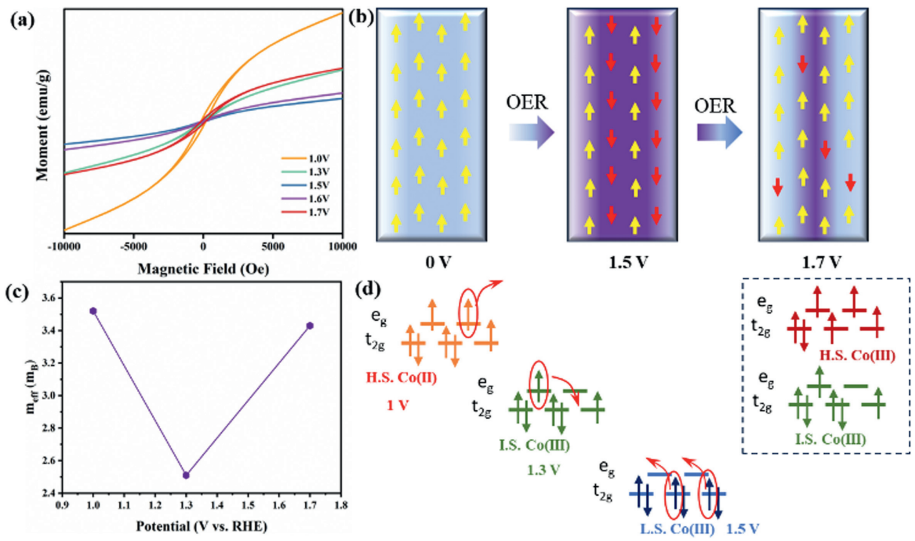

Fig. 4. (a) The magnetization versus magnetic field curve of CoO under different potentials. (b) The schematic diagram of magnetic features evolution under 0, 1.5, and 1.7 V. (c) Effective magnetic moment changes under different potentials. (d) Electron spin state of Co and the electron transition schematic diagram during OER process.

reflect as HS/IS Co(III). At this stage, the materials show ferromagnetism again.

This work constructed the relationship between the valence statements and the electron spin statement. And also form a new strategy to observe OER from the magnetism aspect of a catalyst. More importantly, it revealed that behind the surface reconstruction of the catalyst, electron reassignment is the main factor to affects OER performance. It provides a new and effective method to reveal the magnetic 3d transition metal catalyst evolution during the electrochemical reactions. A similar pathway can be extended to the study of ORR, HER, and even CORR.

Declaration of competing interest

The authors declare that they have no known competing financial interests or personal relationships that could have appeared to influence the work reported in this article.

CRediT authorship contribution statement

Yanjie Li: Data curation, Investigation, Writing – original draft. **Siqi Meng:** Data curation, Visualization. **Jiaqi Hu:** Conceptualization, Investigation. **Ze Gao:** Formal analysis, Validation. **Hongji Xu:** Methodology, Validation, Writing – review & editing. **Rui Gao:** Project administration, Supervision, Writing – review & editing. **Ming Feng:** Funding acquisition, Supervision, Writing – review & editing.

Acknowledgments

This work is financially supported by the National Natural Science Foundation of China (No. 52171210), and the Program for the Development of Science and Technology of Jilin Province (Nos. 20240101004JC, 20220201130GX, and 20240402072GH). Allocation of beamtime at 4B9A, BSRF, Beijing, China, is gratefully acknowledged. The authors would like to thank Dr. Zhongjun Chen and Zhonghua Wu for their help in the X-ray based measurement and analysis.

Supplementary materials

Supplementary material associated with this article can be found, in the online version, at doi:10.1016/j.cclet.2024.109872.

References

[1] F. Cao, M. Li, Y. Hu, et al., Chem. Eng. J. 472 (2023) 144970.
[2] M. Bajdich, M. García-Mota, A. Vojvodic, et al., J. Am. Chem. Soc. 135 (2013) 13521–13530.
[3] Y. Huang, L.W. Jiang, H. Liu, et al., Chem. Eng. J. 441 (2022) 136121.
[4] Y.G. Zhu, C.Q. Shang, Z.Y. Wang, et al., Rare Met 40 (2021) 90–95.
[5] H. Bai, J. Feng, D. Liu, et al., Small 19 (2023) e2205638.
[6] Z. Li, Z. Wang, S. Xi, et al., ACS Nano 15 (2021) 7105–7113.
[7] T. Wu, X. Ren, Y. Sun, et al., Nat. Commun. 12 (2021) 3634.
[8] X. Zheng, J. Yang, Z. Xu, et al., Angew. Chem. Int. Ed. 61 (2022) e202205946.
[9] L.Y. Zhang, T. Zeng, L. Zheng, et al., Adv. Powder. Mater. 2 (2023) 100131.
[10] Z.P. Wu, X.F. Lu, S.Q. Zang, et al., Adv. Funct. Mater. 30 (2020) 1910274.
[11] H. Wang, S. Zhu, J. Deng, et al., Chin. Chem. Lett. 32 (2021) 291–298.
[12] F. Zoller, S. Häringer, D. Boehm, et al., Small 17 (2021) 2007484.
[13] R. Yuan, H. Li, X. Yin, et al., J. Materiomics 7 (2021) 640–647.
[14] X. Wang, Z. Mao, X. Mao, et al., Adv. Sci. 10 (2023) 2206204.
[15] Y. Li, Q. Zhang, X. Zhao, et al., Adv. Funct. Mater. (2023) 2214124.
[16] M. Wu, G. Zhang, H. Tong, et al., Nano Energy 79 (2021) 105409.
[17] M. Chen, D. Liu, B. Zi, et al., J. Energy Chem. 65 (2022) 405–414.
[18] B. Zhang, L. Wang, Z. Cao, et al., Nat. Catal. 3 (2020) 985–992.
[19] X.X. Li, X.C. Liu, C. Liu, et al., Tungsten 5 (2023) 100–108.
[20] J. Sun, N. Guo, T. Song, et al., Adv. Powder Mater. 1 (2022) 100023.
[21] S. Gupta, A. Yadav, S. Bhartiya, M.K. Singh, Nanoscale 10 (2018) 8806–8819.
[22] W. Hu, M. Zheng, H. Duan, et al., Chin. Chem. Lett. 33 (2022) 1412–1416.
[23] T. Ling, D.Y. Yan, Y. Jiao, et al., Nat. Commun. 7 (2016) 12876.
[24] H.W. Jee, K.J. Paeng, N. Myung, et al., J. Electrochem Soc. 164 (2017) D861.
[25] X. Wang, C. Yang, X. Wang, et al., ACS Sustain. Chem. Eng. 9 (2021) 137–146.
[26] K. Du, L. Zhang, J. Shan, et al., Nat. Commun. 13 (2022) 5448.
[27] W. Kang, R. Wei, H. Yin, et al., J. Am. Chem. Soc. 145 (2023) 3470.
[28] W. Guo, H. Luo, D. Fang, et al., J. Energy Chem. 70 (2022) 373–381.
[29] W. Zhang, R. Gao, J. Chen, et al., ACS Appl. Mater. Interfaces 14 (2022) 28965–28976.
[30] N. Ma, H. Xie, T. Yang, et al., Surf. Sci. 711 (2021) 121862.
[31] Z. Kou, Y. Yu, X. Liu, et al., ACS Catal. 10 (2020) 4411–4419.
[32] M. Yu, E. Budiyanto, H. Tuysuz, et al., Angew. Chem. Int. Ed. 61 (2022) e202103824.
[33] J. Qi, X. Yang, P.Y. Pan, et al., Environ. Sci. Technol. 56 (2022) 5200–5212.
[34] Y. Zheng, R. Gao, L. Zheng, et al., ACS Catal. 9 (2019) 3773–3782.
[35] L.W. Jiang, Y. Huang, Y. Zou, et al., Adv. Energy Mater. 12 (2022) 2202351.
[36] P. Ye, K. Fang, H. Wang, et al., Nat. Commun. 1 (2024) 1012.
[37] G. Sun, R. Gao, H. Jiao, et al., Adv. Mater. 34 (2022) 2201838.
[38] P. Wang, T. Wang, M. Xu, et al., Chin. Chem. Lett. (2023) 108930.
[39] Z. Xiao, Y. Huang, C. Dong, et al., J. Am. Chem. Soc. 142 (2020) 12087.
[40] P.A. Kempler, A.C. Nielander, Nat. Commun. 14 (2023) 1158.
[41] X. Ye, J. Fan, Y. Min, et al., Nanoscale 13 (2021) 14854–14865.
[42] H. Liu, Y. Liu, S. Mehdi, et al., Adv. Sci. 8 (2021) e2101314.
[43] Y. Wang, W. Suo, Y. Huang, et al., J. Alloys Compd. 928 (2022) 167210.
[44] Y.C. Huang, W. Chen, Z. Xiao, et al., J. Phys. Chem. Lett. 13 (2022) 8386–8396.
[45] M.A. El-Jemni, H.S. Abdel-Samad, A.S. Essa, et al., Electrochim. Acta 313 (2019) 403–414.
[46] Q.L. Dai, J.K. Tang, Nanoscale 5 (2013) 7512–7519.
[47] Z. Chen, H. Sun, X. Zhou, et al., J. Materiomics 8 (2022) 1141–1148.
[48] S. Ponath, M. Menger, L. Grothues, et al., Angew. Chem. Int. Ed. 61 (2022) e202214643.
[49] M. Mozaffari, Y. Hadadian, A. Aftabi, et al., J. Magn. Magn. Mater. 354 (2014) 119–124.